



ML Prediction of Global Ionospheric TEC Maps

Journal:	<i>Transactions on Geoscience and Remote Sensing</i>
Manuscript ID	TGRS-2021-04001
Manuscript Type:	Regular paper
Date Submitted by the Author:	29-Dec-2021
Complete List of Authors:	Liu, Lei; University of Colorado at Boulder, Ann and H. J. Smead Aerospace Engineering Sciences Department; University of Michigan, Department of Climate and Space Sciences and Engineering Morton, Yu; University of Colorado Boulder, Smead Aerospace Engineering Sciences Department Liu, Yunxiang; University of Colorado Boulder, Ann and H.J. Smead Aerospace Engineering Sciences
Keywords:	GNSS Data, Atmosphere
Note: The following files were submitted by the author for peer review, but cannot be converted to PDF. You must view these files (e.g. movies) online.	
Movie S1-storm_time.gif Movie S2-quiet_time.gif	

SCHOLARONE™
Manuscripts

ML Prediction of Global Ionospheric TEC Maps

Lei Liu^{ID}, Y. Jade Morton^{ID}, *Fellow, IEEE*, and Yunxiang Liu^{ID}

Abstract—This paper applies the convolutional long short-term memory (convLSTM)-based machine learning (ML) models to forecast global ionospheric total electron content (TEC) maps with up to 24 hours of lead time at a 1-hour interval. Four convLSTM-based models were investigated, and the one that implements the L_1 loss function and the residual prediction strategy demonstrates the best performance. The convLSTM models are trained and evaluated using Centre for Orbit Determination in Europe (CODE) global TEC maps over a period of nearly seven years from October 19, 2014 to July 21, 2021. Results show that the best convLSTM model outperforms the 1-day predicted global TEC products released by CODE analysis center (c1pg) and persistence models under various levels of solar and geomagnetic activities, except for a lead time beyond 8 hours during the storm time where the c1pg has slightly better performance. The convLSTM forecasting performance degrades as the lead time increases.

Index Terms—Ionospheric total electron content (TEC), machine learning (ML) prediction, convolutional long short-term memory (convLSTM)

I. INTRODUCTION

IONOSPHERIC total electron content (TEC) refers to the total number of electrons integrated along a radio wave propagation path within a unit cross section area (unit: TECU, $1\text{TECU}=10^{16}\text{electrons}/m^2$). Satellite navigation and radio communication system performance are degraded when radio waves traverse the ionosphere in the presence of the ionospheric TEC gradients and plasma density irregularities [1], [2], [3]. Reliable specification and prediction of ionospheric TEC are not only helpful for mitigating uncertainties in global navigation satellite system (GNSS)-based position, navigation, and timing (PNT) services, but also for timely warning of space weather activities [4], [5], [6].

Ionospheric TEC maps can be constructed using networks of dual-frequency GNSS receiver measurements [7], [8], [9], [10]. A major challenge is to forecast global TEC maps accurately, especially for relatively long lead times such as one day. This is due to the ionospheric dynamic nature driven by solar-geomagnetic activities and multi-scale ionospheric processes [11], [12], [13], [14]. Numerous approaches have been developed to forecast global ionospheric TEC maps. For example, Schaer [7] presented the least square collocation method to extrapolate spherical harmonic (SH) coefficients that were used for constructing TEC maps. The resulting global TEC maps are one of the international GNSS service

(IGS) official ionospheric products released by the Centre for Orbit Determination in Europe (CODE). García-Rigo et al. [15] developed a global TEC prediction model based on the discrete cosine transform. Wang et al. [16] developed an adaptive autoregressive model to predict the SH coefficients and reproduce the global TEC map by using the predicted SH coefficients.

In recent years, machine learning (ML) techniques have become a promising and effective tool to predict global TEC maps. For example, Perez [17] predicted global ionospheric TEC based on a fully connected neural network (NN). The model was evaluated by the position error in GNSS single frequency ionospheric delay correction. However, the equatorial ionization anomalies (EIA) were not well captured by the predicted global TEC maps. Lee et al. [18] predicted daily global TEC maps with a 2-hour interval using an image-based conditional generative adversarial network (GAN). The results demonstrated that the model had slightly better performance compared to the CODE prediction products. However, this performance comparison may not be fair because the training data used in Lee et al. [18] was obtained from the IGS final TEC products that are weighted mean TEC values of four ionospheric analysis centers (JPL, CODE, ESA and UPC), while the CODE predicted TEC maps are obtained only from the CODE TEC products. Liu et al. [19] applied the long short-term memory (LSTM) network to forecast SH coefficients for the next two hours by incorporating SH coefficients, solar data, and geomagnetic data. The model showed competitive prediction performance compared to traditional models, while further study is still needed to extend its prediction lead time. Boulch et al. [20] presented convolutional recurrent neural networks (RNN) for global ionospheric TEC prediction using CODE TEC data from 2014 to 2016. Their results showed that the prediction performance was comparable with that of the autoregressive (AR), autoregressive moving average (ARMA), and the radial basis function NN.

This paper extends the work of Boulch et al. [20] to implement four variations of an image-based convolutional long short-term memory (convLSTM) ML algorithm to forecast global TEC maps with a lead time up to 24 hours at a 1-hour interval. The CODE TEC maps over a 7-year span from 2014 to 2021 collected under various levels of solar and geomagnetic activities are used in the implementations. The best performing model among the four implementations is selected based on a set of skill scores, and is compared against two conventional prediction models under various levels of solar and geomagnetic conditions to demonstrate the superior performance.

L. Liu, Y. Morton and Y. Liu are with the Ann & H. J. Smead Department of Aerospace Engineering Sciences, University of Colorado Boulder, Boulder, CO, USA. E-mail: lei.liu@colorado.edu, jade.morton@colorado.edu, yuli9721@colorado.edu. This work was supported by DARPA grant #DI 9AC00009

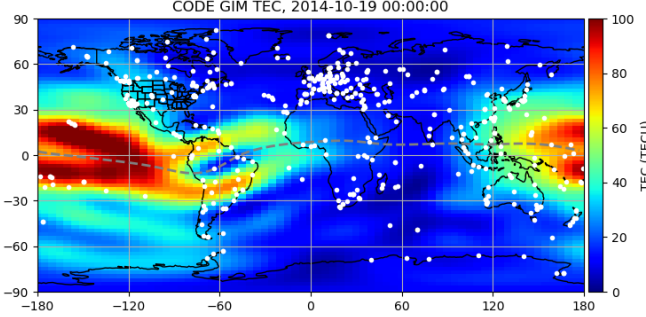
1
94 Main contributions of this work compared to that of Boulch
95 et al. [20] include the use of an extensive global TEC data set
96 spanning 7 years, the improved time resolution from 2 hours
97 to 1 hour, different data segmentation for training, testing,
98 and validation, the prediction of residual TEC maps between
99 consecutive days at the same hour, as well as the utilization of
100 batch normalization [21] and dropout [22], and comprehensive
101 performance evaluations.

10 This paper is organized as follows. Section II describes the
11 data used in the study, the specific ML algorithm implemen-
12 tations, and evaluation metrics. Section III presents qualitative
13 and statistical evaluation. Section IV concludes the study.

II. DATA AND METHODOLOGY

A. Data Description

18 Global ionospheric TEC data used in this study are obtained
19 from the CODE Global Ionosphere Maps (GIM). CODE's
20 GIMs are gridded TEC maps that are represented by the
21 spherical harmonic function derived from worldwide ground-
22 based GNSS measurements [7]. The temporal resolution of the
23 CODE's GIM has been updated from 2 hours to 1 hour since
24 October 19, 2014. Figure 1 shows an example of the CODE
25 TEC map at 12:00 UT on October 19, 2014. Locations of
26 IGS GNSS receivers, from which measurements were used
27 to produce this map, are marked by white colored dots. The
28 spatial resolution is 2.5° latitude by 5° longitude (71 in
29 height by 73 in width). To ease the ML training process, the
30 dimension of the TEC map is resized from 71×73 to 73×73
31 by padding zero values over north and south poles. The grid
32 size remains $2.5^\circ \times 5^\circ$.



44 Fig. 1. An example of the global TEC map from the CODE GIM at 12:00
45 UT on October 19, 2014. White colored dots represent GNSS receivers used
46 to generate the TEC map. The dashed grey line represents the geomagnetic
47 equator. The color scale indicates the value in TECU.

48 The hourly CODE TEC data used in this study are from
49 October 19, 2014 to July 21, 2021, which are divided into
50 training (60%), validation (20%), and testing (20%) sets.
51 To ensure that all three sets of data contain low, moderate,
52 and strong solar activity levels and capture seasonal effects,
53 we adopt the following novel data segmentation strategy as
54 illustrated in Figure 2. The dataset is divided into multiple
55 groups, where each group contains 50 days of data. For each
56 group (see the bottom panel of Figure 2), the data in the first
57 30 days (yellow shaded area) are used for training, and the
58 next 10 days (red shaded area) and last 10 days (cyan shaded

59 area) are used for validation and testing, respectively. Based
60 on this criteria, 335784, 11760 and 11760 data samples are
61 obtained for training, validation, and testing, respectively.

134

135

136

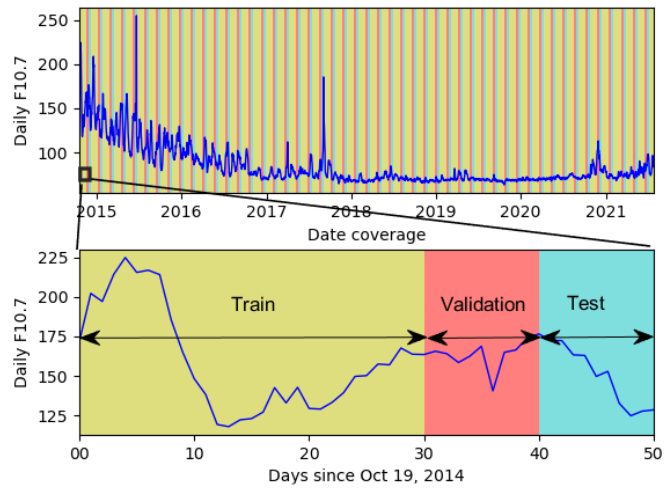


Fig. 2. Top: Data ranging from October 19, 2014 to July 21, 2021 are used. Each group (50 days) in the dataset is divided into training (yellow shaded area), validation (red shaded area) and testing (cyan shaded area) subsets, respectively. Bottom: A close-up view of one group of data starting on Oct 19, 2017. The F10.7 indicator (blue line) shows the daily solar activity level.

B. convLSTM ML Algorithm

The convLSTM architecture is capable of learning features
137 from a spatiotemporal sequence. It has been successfully
138 applied in many fields of multi-dimensional spatiotemporal
139 predictions [23], [24], [25]. In this study, the convLSTM layer
140 is used as the core module to predict global TEC maps.
141 Detailed structure of the convLSTM module can be found in
142 Figure S1 of the supporting information (SI) file.

143 Figure 3 illustrates the convLSTM-based ML architecture,
144 which consists of four parts: input, encoder, decoder, and
145 output. The dimensions of the input and output maps are
146 the same (73×73). The inputs consist of 24 consecutive TEC
147 maps ($X_1, X_2, \dots, X_{23}, X_{24}$) with a 1-hour interval. These maps
148 are fed into 3 encoder blocks. Each encoder block includes a
149 convolutional (conv) layer and a convLSTM layer. The conv
150 layer and the convLSTM layer are used for down-sampling
151 and learning spatiotemporal features, respectively. Similarly,
152 3 decoder blocks are composed of deconvolutional (deconv)
153 and convLSTM layers. The hidden features generated by
154 the encoder blocks are used as the inputs for the decoder
155 blocks. The encoder parts are then unfolded using the decoder
156 blocks to predict 24 future maps, which are elements of the
157 output ($\hat{X}_{25}, \hat{X}_{26}, \dots, \hat{X}_{47}, \hat{X}_{48}$) shown in Figure 3. Detailed
158 descriptions of this architecture can be found in Shi et al.
159 [23] and Liu et al. [25]. Here, two prediction strategies are
160 implemented to predict global TEC maps.

- 161 1) **Residual prediction:** The output ($\hat{X}_{25}, \hat{X}_{26}, \dots, \hat{X}_{47}, \hat{X}_{48}$)
162 is the TEC residual between the map at time t and $t-24$,
163 namely,

$$\hat{X}_t = TEC(t) - TEC(t-24) \quad (1)$$

where $t=25, 26, \dots, 47, 48$. Once the TEC residual is produced by the ML model, the predicted TEC map is obtained by adding the background TEC from the previous day to the predicted TEC residual to obtain the predicted TEC.

2) **Direct prediction:** TEC maps are predicted directly by the ML model. This means the model output ($\hat{X}_{25}, \hat{X}_{26}, \dots, \hat{X}_{47}, \hat{X}_{48}$) is the hourly predicted TEC map for the next day.

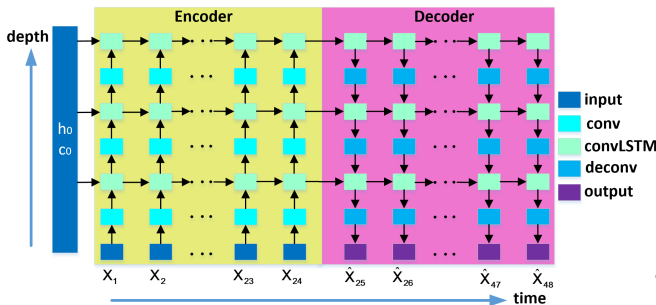


Fig. 3. Illustration of ML architecture. Input: $X_1, X_2, \dots, X_{23}, X_{24}$ are input TEC maps from the past 24 hours. Output: $\hat{X}_{25}, \hat{X}_{26}, \dots, \hat{X}_{47}, \hat{X}_{48}$ are 24 predicted targets in the next 24 hours. The targets can be either TEC maps or TEC map residuals, depending on the prediction strategy. Conv: convolutional layer. ConvLSTM: convolutional LSTM layer. Deconv: deconvolutional layer.

The parameter configurations of this architecture, such as filter number, filter size, stride, and padding, as well as the height and width of each output matrix after operations of conv, convLSTM and deconv layers, can be found in Table I.

C. Evaluation Metrics

To quantify the prediction performance, the following metrics are utilized:

$$\left\{ \begin{array}{l} ME = \frac{1}{N} \sum_{i=1}^N (\hat{x}_i - x_i) \\ RMSE = \sqrt{\frac{1}{N} \sum_{i=1}^N (\hat{x}_i - x_i)^2} \\ CC = \frac{\text{cov}(\hat{x}_i, x_i)}{\sigma_{\hat{x}_i} \cdot \sigma_{x_i}} \end{array} \right. \quad (2)$$

where ME is the mean error; $RMSE$ is the root mean square error; MAE is mean absolute error; CC is the Pearson correlation coefficient. N is number of the TEC bins. x_i and \hat{x}_i are the gridded TEC values of the ground truth and prediction, respectively. $\text{cov}(\hat{x}_i, x_i)$ is the covariance between \hat{x}_i and x_i . $\sigma_{\hat{x}_i}$ and σ_{x_i} are the standard deviations of \hat{x}_i and x_i , respectively.

III. RESULTS AND DISCUSSIONS

The models are implemented in Python with the PyTorch package and trained on a server with two 12GB NVIDIA TITAN GPUs, dual 10-core Intel(R) Xeon(R) Silver 4114 CPUs @ 2.20GHz, and 251 GB of RAM. In this study, the Adam optimizer is employed [26]. The Leaky rectified linear unit (ReLU) activation function with a leaky value of 0.2 is used to avoid dead neurons in the networks caused by

conventional ReLU due to the “dying ReLU problem” [27]. Batch normalization is implemented to accelerate training by reducing internal covariate shift [21]. Dropout regularization is used to reduce overfitting and to improve the model generalization ability [22]. The learning rate and batch size are set to 5e-5 and 72 based on trial-and-error runs, respectively.

Four convLSTM-based models with different combinations of loss functions (L_1 and L_2) and prediction strategies (direct and residual predictions, see details in subsection II-B) are implemented. These four models are shown in Table II.

Table III shows performance comparison of the four models on training, validation and testing sets, respectively. Model C has the best performance with lower $RMSE$ and MAE values and higher CC values compared to the other three models on all data sets. This may be due to two reasons. First, the L_1 loss is capable of forcing the model to obtain accurate predictions that are far away from the mean values, which is especially helpful for predicting TEC values with large magnitudes, such as the TEC peaks around the local noon sector and equatorial ionization anomaly (EIA) crest regions. Second, the utilization of residual prediction strategy removes the background ionosphere, forcing the model to only focus on the smaller range associated with deviations of the ionosphere. Because of the better performance of model C, ML prediction results and performances discussed in the remaining paper are all obtained from model C. In the remaining paper, the convLSTM refers to model C.

A. A Qualitative Case Study

In this case study, we compare the convLSTM prediction with that of c1pg during the main phase of a storm event that occurred during 10:00-13:00 UT on May 6, 2015, when $KP \approx 3 - 5.3$ and $F10.7=138.6$. The c1pg is 1-day predicted global ionospheric TEC map released by CODE analysis center, and it is produced based on the extrapolation of spherical harmonic coefficients [7]. Figure 4 shows the 1-hour interval TEC maps predicted by the convLSTM and c1pg models. The codg refers to CODE’s GIM, which is the ground truth. The plots show that the predicted TEC maps from convLSTM and c1pg agree well with the truth. In particular, large-scale ionospheric patterns, such as the daytime EIA crests, are well-preserved. We can also observe from Figure 4 that the predicted TEC maps from convLSTM are closer to the truth than those from c1pg. For example, The TEC enhancement shown near $30^{\circ}\text{E}-80^{\circ}\text{E}$ longitude and $40^{\circ}\text{S}-60^{\circ}\text{S}$ latitude of codg is well reproduced in the convLSTM model (see red circles in the middle column of Figure 4), while the c1pg fails to capture it.

Figure 5 shows the difference between the truth and predicted maps during the main phase of the storm event. The magnitude of the TEC difference maps from convLSTM is clearly smaller than that from c1pg. This indicates the convLSTM ML model has a better prediction performance than c1pg. In addition, an example during geomagnetic quiet time also corroborates the same conclusion that the convLSTM has a better performance (see Figure S2 and Movie S2 in the SI).

TABLE I

DETAILED PARAMETER CONFIGURATIONS OF THE MODEL ARCHITECTURE. I AND O REPRESENT INPUT AND OUTPUT OF EACH MODULE, RESPECTIVELY.

Network	Module	Filter number		Filter size	Stride	Padding	Height and width	
		I	O				I	O
Encoder	conv	1	8	3x3	2x2	1x1	73x73	37x37
	convLSTM	8	16	5x5	1x1	2x2	37x37	37x37
	conv	16	16	3x3	2x2	1x1	37x37	19x19
	convLSTM	16	32	5x5	1x1	2x2	19x19	19x19
	conv	32	32	3x3	2x2	1x1	19x19	10x10
	convLSTM	32	32	5x5	1x1	2x2	10x10	10x10
Decoder	convLSTM	32	32	5x5	1x1	2x2	10x10	10x10
	deconv	32	32	3x3	2x2	1x1	10x10	19x19
	convLSTM	32	32	5x5	1x1	2x2	19x19	19x19
	deconv	32	32	3x3	2x2	1x1	19x19	37x37
	convLSTM	32	16	5x5	1x1	2x2	37x37	37x37
	deconv	16	8	3x3	2x2	1x1	37x37	73x73
	conv	8	1	1x1	1x1	0x0	73x73	73x73

TABLE II

FOUR CONVLSTM-BASED MODELS IMPLEMENTED IN THIS STUDY BY COMBINING DIFFERENT LOSS FUNCTIONS AND PREDICTION STRATEGIES.

Model	Loss function	Prediction strategy
A	L_1	direct prediction
B	L_2	direct prediction
C	L_1	residual prediction
D	L_2	residual prediction

B. Statistical Evaluation

A statistical evaluation is also conducted under varying levels of solar and geomagnetic activities. The convLSTM is compared to c1pg and to a persistence model. The persistence model assumes that the predicted TEC map at time t is the same as that at $t-24$. F10.7 and KP parameters are used as indicators of solar and geomagnetic levels, respectively. Table IV shows the definitions of the high/low solar activity and geomagnetic storm/quiet levels.

Figure 6 shows comparison results under low (a) and high (b) solar activities on the testing set as functions of the lead time. Four metrics are plotted for each solar activity level. The following observations are obtained:

(1) The convLSTM model shows better prediction performance compared to c1pg and persistence models for all lead times and with all metrics.

(2) A slight performance degradation is observed for convLSTM under high solar activities compared to the ones under low solar activities. For example, the RMSE increases from 1.78 to 3.31 TECU. Such levels of prediction error difference are within the margin of the truth precision, which is around 2-8 TECU [8], [28], [29].

(3) The predictive capability of the convLSTM degrades with increasing lead time, while c1pg and persistence models show almost no dependence on the lead time.

Figure 7 compares the performance using data collected under geomagnetic quiet (a) and storm (b) conditions. We have the

following observations:

(1) The convLSTM model shows better performance compared to other two models for all lead times tested under geomagnetic quiet conditions.

(2) During geomagnetic storms, the prediction performance of the convLSTM remains the best when the lead time is smaller than 8 hours. The c1pg shows a slightly better performance compared to convLSTM when the lead time is longer than 8 hours, and there is a notable performance improvement with increasing lead time under geomagnetic storm conditions. Additional investigations may be required to study this behavior.

(3) For the convLSTM model, the minimum RMSE errors for quiet/storm time are 0.81/1.28 TECU, and the maximum RMSE errors for quiet/storm time are 2.15/3.26 TECU. This indicates that the RMSE degradation of convLSTM is not significant under geomagnetic storm conditions. Similar observations can be found from other metrics. This may be due to the fact that some features from geomagnetic activities have already been contained in the 24 input TEC maps of the convLSTM model, thus leading to an insignificant performance degradation under storm conditions.

Figure 8 plots the ME (top panel) and RMSE (bottom panel) errors of the convLSTM, c1pg and persistence models as functions of latitude. The convLSTM has the smallest ME error. Moreover, the ME errors of the convLSTM and persistence model stabilize around zero across all latitudes. This indicates that there are no systematic biases in the TEC maps predicted by convLSTM and the persistence models. However, c1pg underestimates/overestimates the predicted TEC over the mid-high latitude of the southern/northern hemispheres. In terms of RMSE errors, the convLSTM shows an improved performance over the other two models over various latitudes. In addition, the RMSE errors of three models show obvious latitudinal dependence, and two peaks are located near geographic latitude of 10°S and 20°N, respectively. This is probably related to strong ionospheric gradients around the daily EIA crest.

TABLE III

DETAILED PARAMETER CONFIGURATIONS OF THE MODEL ARCHITECTURE. I AND O REPRESENT INPUT AND OUTPUT OF EACH MODULE, RESPECTIVELY.

Model	RMSE (TECU)			MAE (TECU)			CC		
	Train	Validation	Test	Train	Validation	Test	Train	Validation	Test
A	1.90	1.97	1.94	1.22	1.25	1.24	0.97	0.97	0.96
B	2.0	2.03	2.01	1.34	1.35	1.33	0.96	0.96	0.96
C	1.72	1.90	1.88	1.12	1.20	1.20	0.98	0.97	0.97
D	2.06	2.04	2.03	1.35	1.33	1.33	0.96	0.97	0.96

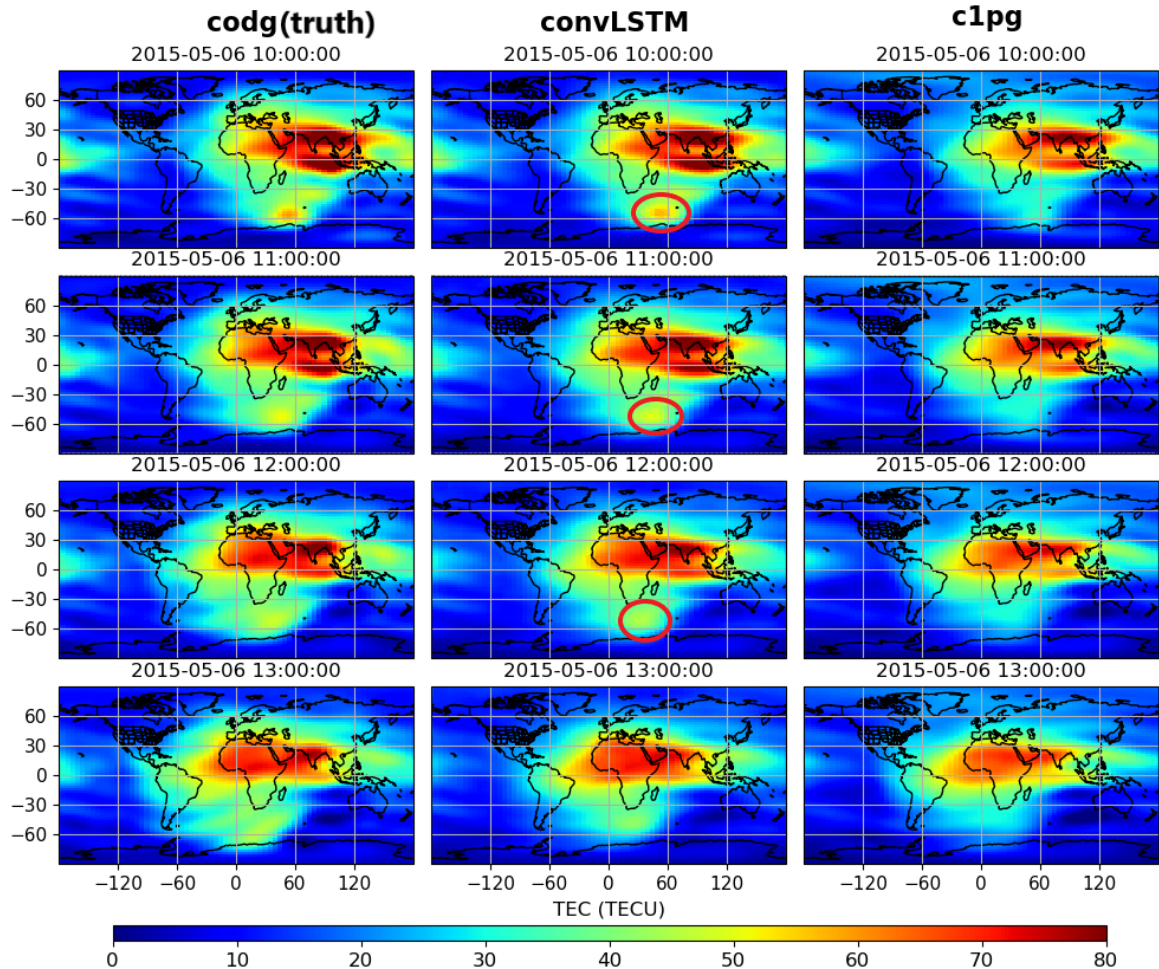


Fig. 4. An example of the predicted global TEC maps at a 1-hour interval during the main phase of one geomagnetic storm event (10:00-13:00 UT, May 6, 2015), where the KP varies from 3.7 to 5.3, and F10.7 is 138.6. The left column represents the TEC maps from codg, which are the ground truth. The middle and right columns represent the predicted TEC maps from convLSTM and c1pg, respectively. Full sets of the predicted global TEC maps with lead times up to 24 hours are available in Movie S1 of the SI.

TABLE IV

THE THRESHOLD OF DIFFERENT SOLAR AND GEOMAGNETIC ACTIVITY LEVELS.

Indicators	Threshold	Defined levels
F10.7	$F10.7 \geq 120$	high solar activity
	$F10.7 < 120$	low solar activity
KP	$KP > 4$	geomagnetic storm
	$KP \leq 4$	geomagnetic quiet

IV. CONCLUSIONS

This paper discusses convLSTM-based ML algorithms implemented to predict daily global TEC maps using CODE data

collected from October 19, 2014 to July 21, 2021. Among four different implementations, the convLSTM model that combines the L_1 loss function and residual prediction strategy shows the best performance. This best performing convLSTM model also shows more accurate prediction compared to c1pg, which is 1-day predicted global TEC product released by CODE analysis center. Moreover, prominent structures, such as typical EIA and TEC enhancement over southern hemisphere, are successfully reproduced by the convLSTM model.

Our statistical evaluation shows that the convLSTM model significantly outperforms both the c1pg and persistence models

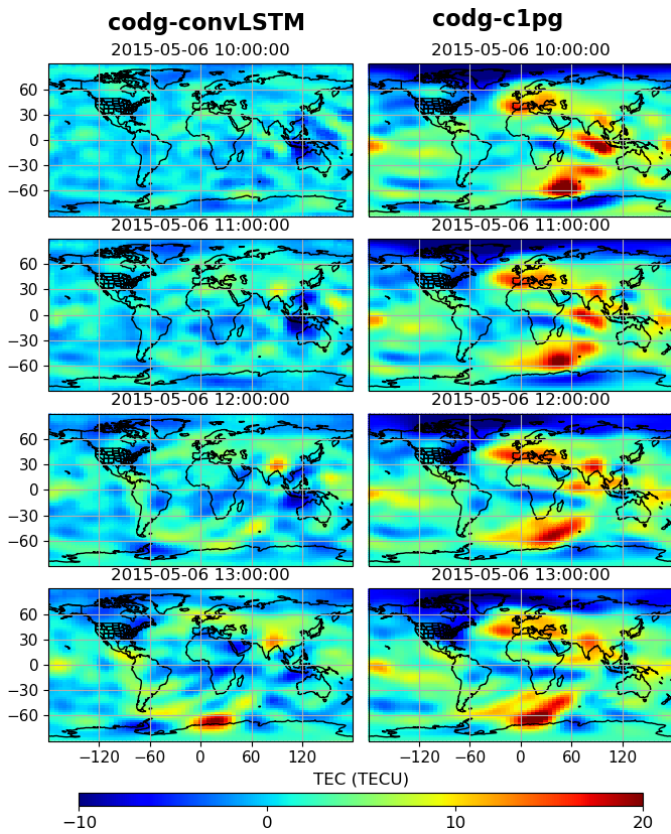


Fig. 5. Comparison of the TEC difference maps between codg and convLSTM. Left column: codg minus convLSTM. Right column: codg minus c1pg.

under all levels of solar activities for all lead times tested and at all latitudes. A slight performance degradation is observed for convLSTM under high solar activities compared to the ones under low solar activities. When compared to c1pg and persistence models, the convLSTM model shows better performance for all lead times tested under geomagnetic quiet conditions and for lead times below 8 hours of storm conditions. For lead times beyond 8 hours during the storm times, the c1pg has slightly better performance. The convLSTM model shows an insignificant performance degradation during the storm time compared to the quiet time. The convLSTM model degrades with the increasing lead time, while only a very weak time dependence is observed in results from the c1pg and persistence models.

ACKNOWLEDGMENT

This project is sponsored by DARPA DSO Space Environment Exploitation (SEE) Program grant #DI 9AC00009. The CODE GIM data are available from the Crustal Dynamics Data Information System (CDDIS) (<https://cddis.nasa.gov/>) via registration. Solar and Geomagnetic data are obtained from the OMNI Goddard Flight Center (<https://omniweb.gsfc.nasa.gov/>). The authors acknowledge the SWAMI server at the Space Weather Technology, Research and Education Center (SWx-TREC), University of Colorado, Boulder for providing high-performance computing that contributed to this work.

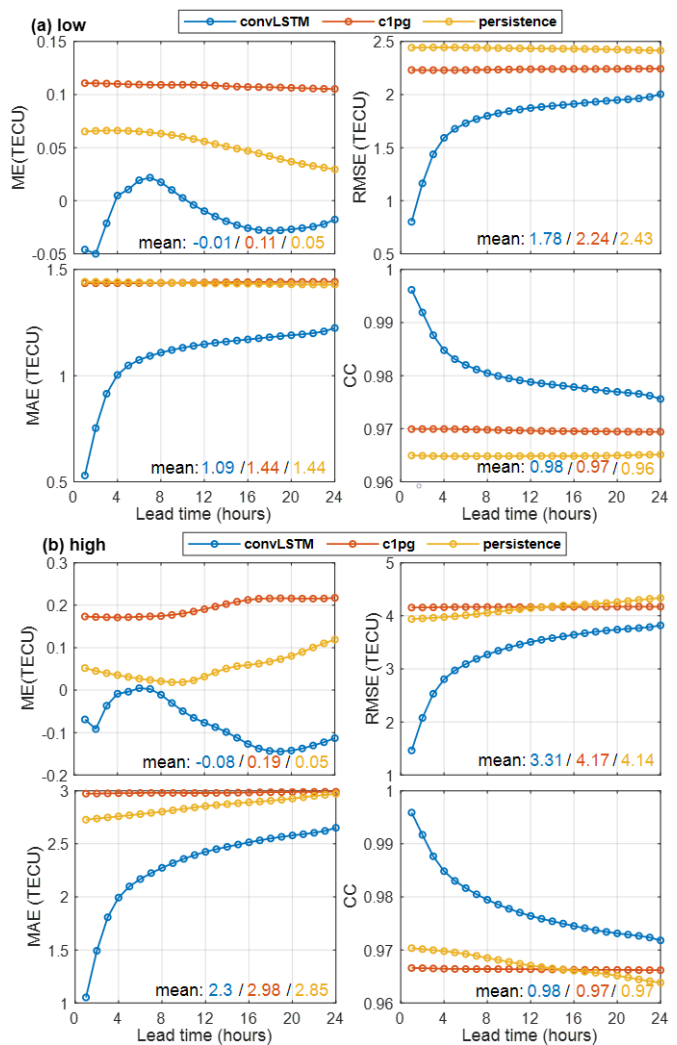


Fig. 6. Performance comparison among convLSTM, c1pg, and the persistence models under the low (a) and high (b) solar activity levels on the testing set. Blue, red, and orange curves in each panel refer to metrics obtained from convLSTM, c1pg, and persistence models, respectively. Mean metrics across all lead time are illustrated at the bottom of each panel.

REFERENCES

- [1] S. Basu, S. Basu, E. MacKenzie, W. Coley, J. Sharber, and W. Hoegy, "Plasma structuring by the gradient drift instability at high latitudes and comparison with velocity shear driven processes," *Journal of Geophysical Research: Space Physics*, vol. 95, no. A6, pp. 7799–7818, 1990.
- [2] K. C. Yeh and C.-H. Liu, "Radio wave scintillations in the ionosphere," *Proceedings of the IEEE*, vol. 70, no. 4, pp. 324–360, 1982.
- [3] K. S. Jacobsen and Y. L. Andalsvik, "Overview of the 2015 st. patrick's day storm and its consequences for rtk and ppp positioning in norway," *Journal of Space Weather and Space Climate*, vol. 6, p. A9, 2016.
- [4] J. A. Klobuchar, "Ionospheric time-delay algorithm for single-frequency gps users," *IEEE Transactions on aerospace and electronic systems*, no. 3, pp. 325–331, 1987.
- [5] N. Jakowski, Y. Béniguel, G. De Franceschi, M. H. Pajares, K. S. Jacobsen, I. Stanislawska, L. Tomaszik, R. Warnant, and G. Wautlet, "Monitoring, tracking and forecasting ionospheric perturbations using gnss techniques," *Journal of Space Weather and Space Climate*, vol. 2, p. A22, 2012.
- [6] Y. J. Morton, Z. Yang, B. Breitsch, H. Bourne, and C. Rino, "Ionospheric effects, monitoring, and mitigation techniques," *Position, Navigation, and Timing Technologies in the 21st Century: Integrated Satellite*

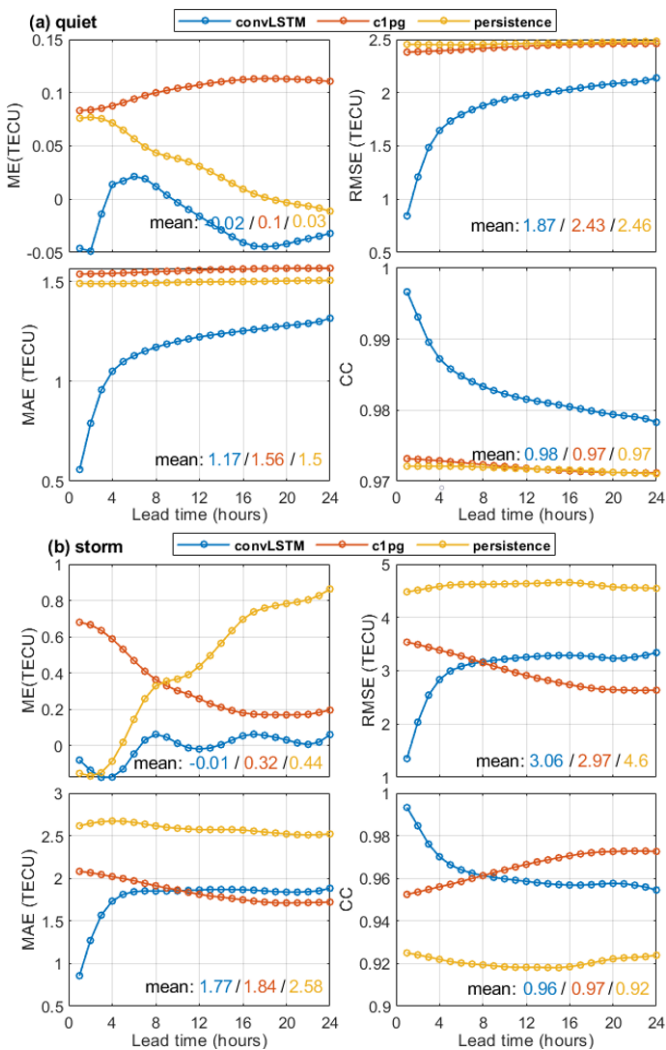


Fig. 7. Performance comparison among convLSTM, c1pg, and persistence models under geomagnetic quiet (a) and storm levels (b) on the testing set.

Navigation, Sensor Systems, and Civil Applications, vol. 1, pp. 879–937, 2020.

[7] S. Schaefer and S. helvétique des sciences naturelles. Commission géodésique, *Mapping and predicting the Earth's ionosphere using the Global Positioning System*. Institut für Geodäsie und Photogrammetrie, Eidg. Technische Hochschule ..., 1999, vol. 59.

[8] M. Hernández-Pajares, J. Juan, J. Sanz, R. Orús, A. García-Rigo, J. Feltens, A. Komjathy, S. Schaefer, and A. Krankowski, “The igs vtec maps: a reliable source of ionospheric information since 1998,” *Journal of Geodesy*, vol. 83, no. 3–4, pp. 263–275, 2009.

[9] Y. Yao, L. Liu, J. Kong, and C. Zhai, “Global ionospheric modeling based on multi-gnss, satellite altimetry, and formosat-3/cosmic data,” *GPS Solutions*, vol. 22, no. 4, pp. 1–12, 2018.

[10] P. Chen, H. Liu, M. Schmidt, Y. Yao, and W. Yao, “Near real-time global ionospheric modeling based on an adaptive kalman filter state error covariance matrix determination method,” *IEEE Transactions on Geoscience and Remote Sensing*, 2021.

[11] S. Cowley, “Magnetosphere-ionosphere interactions: A tutorial review,” *Magnetospheric Current Systems, Geophys. Monogr. Ser.*, vol. 118, pp. 91–106, 2000.

[12] Y. Yao, L. Liu, J. Kong, and C. Zhai, “Analysis of the global ionospheric disturbances of the march 2015 great storm,” *Journal of Geophysical Research: Space Physics*, vol. 121, no. 12, pp. 12–157, 2016.

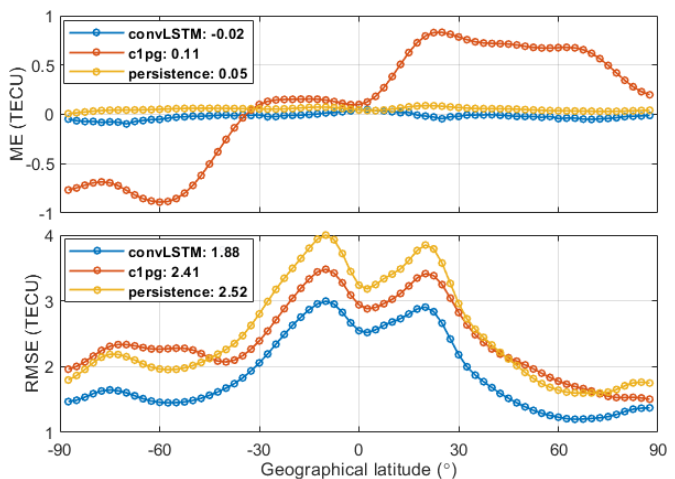


Fig. 8. Latitudinal ME (top panel) and RMSE (bottom panel) errors of three prediction models on the testing set. Blue, red and orange curves represent evaluations metrics from convLSTM, c1pg and persistence models, respectively. The average ME and RMSE values of each model across all latitude are shown in the legend.

[13] E. Camporeale, “The challenge of machine learning in space weather: Nowcasting and forecasting,” *Space Weather*, vol. 17, no. 8, pp. 1166–1207, 2019.

[14] L. Liu, S. Zou, Y. Yao, and E. Aa, “Multi-scale ionosphere responses to the may 2017 magnetic storm over the asian sector,” *GPS Solutions*, vol. 24, no. 1, pp. 1–15, 2020.

[15] A. García-Rigo, E. Monte, M. Hernández-Pajares, J. Juan, J. Sanz, A. Aragón-Angel, and D. Salazar, “Global prediction of the vertical total electron content of the ionosphere based on gps data,” *Radio science*, vol. 46, no. 06, pp. 1–3, 2011.

[16] C. Wang, S. Xin, X. Liu, C. Shi, and L. Fan, “Prediction of global ionospheric vtec maps using an adaptive autoregressive model,” *Earth, Planets and Space*, vol. 70, no. 1, pp. 1–14, 2018.

[17] R. O. Perez, “Using tensorflow-based neural network to estimate gnss single frequency ionospheric delay (iononet),” *Advances in Space Research*, vol. 63, no. 5, pp. 1607–1618, 2019.

[18] S. Lee, E.-Y. Ji, Y.-J. Moon, and E. Park, “One-day forecasting of global tec using a novel deep learning model,” *Space Weather*, vol. 19, no. 1, p. 2020SW002600, 2021.

[19] L. Liu, S. Zou, Y. Yao, and Z. Wang, “Forecasting global ionospheric tec using deep learning approach,” *Space Weather*, vol. 18, no. 11, p. e2020SW002501, 2020.

[20] A. Boulch, N. Cherrier, and T. Castaings, “Ionospheric activity prediction using convolutional recurrent neural networks,” *arXiv preprint arXiv:1810.13273*, 2018.

[21] S. Ioffe and C. Szegedy, “Batch normalization: Accelerating deep network training by reducing internal covariate shift,” in *International conference on machine learning*. PMLR, 2015, pp. 448–456.

[22] S. Wager, S. Wang, and P. S. Liang, “Dropout training as adaptive regularization,” *Advances in neural information processing systems*, vol. 26, pp. 351–359, 2013.

[23] S. Xingjian, Z. Chen, H. Wang, D.-Y. Yeung, W.-K. Wong, and W.-c. Woo, “Convolutional lstm network: A machine learning approach for precipitation nowcasting,” in *Advances in neural information processing systems*, 2015, pp. 802–810.

[24] X. Shi, Z. Gao, L. Lausen, H. Wang, D.-Y. Yeung, W.-k. Wong, and W.-c. Woo, “Deep learning for precipitation nowcasting: A benchmark and a new model,” *arXiv preprint arXiv:1706.03458*, 2017.

- 1
2 [437] [25] L. Liu, Y. J. Morton, and Y. Liu, "Machine learning prediction
3 of storm-time high-latitude ionospheric irregularities from gnss-
4 derived roti maps," *Geophysical Research Letters*, vol. 48, no. 20, p.
5 e2021GL095561, 2021.
- 6 [441] [26] D. P. Kingma and J. Ba, "Adam: A method for stochastic optimization,"
7 *arXiv preprint arXiv:1412.6980*, 2014.
- 8 [443] [27] B. Xu, N. Wang, T. Chen, and M. Li, "Empirical evaluation of rectified
9 activations in convolutional network," *arXiv preprint arXiv:1505.00853*,
10 2015.
- 11 [446] [28] Z. Li, Y. Yuan, N. Wang, M. Hernandez-Pajares, and X. Huo, "Shpts:
12 towards a new method for generating precise global ionospheric tec
13 map based on spherical harmonic and generalized trigonometric series
14 functions," *Journal of Geodesy*, vol. 89, no. 4, pp. 331–345, 2015.
- 15 [450] [29] D. Roma-Dollase, M. Hernández-Pajares, A. Krancowski, K. Kotulak,
16 R. Ghoddousi-Fard, Y. Yuan, Z. Li, H. Zhang, C. Shi, C. Wang
17 et al., "Consistency of seven different gnss global ionospheric mapping
18 techniques during one solar cycle," *Journal of Geodesy*, vol. 92, no. 6,
19 pp. 691–706, 2018.
- 20
21
22
23
24
25
26
27
28
29
30
31
32
33
455
456
457
458
459
460
461
462
463



Lei Liu is a Post-Doc Research Associate for the Satellite Navigation and Sensing Laboratory at the University of Colorado Boulder. He received his Ph.D. in Geodesy and Geomatics from Wuhan University China in 2020. His current research interests are GNSS ionospheric monitoring, modeling, and forecasting of ionospheric TEC and irregularities using machine learning.



Dr. Y. Jade Morton is the Helen and Hubert Croft Professor of Engineering in the Smead Aerospace Engineering Sciences Department at the University of Colorado (CU), Boulder. Her research interests lie at the intersection of satellite navigation technologies and remote sensing of the Earth's ionosphere, atmosphere, and surface. Dr. Morton received her PhD in electrical engineering from Penn State and was an electrical engineering professor at Colorado State University and Miami University prior to join CU in 2017. Dr. Morton is an Institute of Navigation (ION) Thurlow, Burka and Kepler award winner, an IEEE PLANS Kershner award winner, and an IEEE AESS Distinguished Lecturer. She is a fellow of IEEE, the ION, and the Royal Institute of Navigation (RIN).



Yunxiang Liu obtained the PhD from Aerospace Engineering Sciences at the University of Colorado Boulder. He received a B.E. at the University of Electronic Science and Technology of China in 2013 and an M.E. Degree from Nanyang Technological University (NTU) in 2015, both majoring in wireless communications. He worked on machine learning related problems as a research associate at NTU from 2015 to 2016, and later at the Rolls-Royce@NTU Corporate Lab from 2016 to 2017. His research work focuses on applying machine learning techniques to GNSS-based remote sensing tasks.

58
59
60

supporting information (SI)

[ML Prediction of Global Ionospheric TEC Maps]

[Lei Liu, Y. Jade Morton, Yunxiang Liu]

[Ann and H. J. Smead Aerospace Engineering Sciences Department, University of Colorado Boulder,
Boulder, CO, USA]

Contents of this file

Figure S1 to S2.

Introduction

Figure S1. The architecture of convLSTM module.

Figure S2. Predicted global TEC maps for the quiet time.

Mathematics equations about a single convLSTM module (Figure S2) are given below (Shi et al., 2015),

$$\begin{cases} i_t = \sigma(W_{xi} * x_t + W_{hi} * H_{t-1} + W_{ci} \circ C_{t-1} + b_i) \\ f_t = \sigma(W_{xf} * x_t + W_{hf} * H_{t-1} + W_{cf} \circ C_{t-1} + b_f) \\ C_t = f_t \circ C_{t-1} + i_t \circ \tanh(W_{xc} * x_t + W_{hc} * H_{t-1} + b_c) \\ o_t = \sigma(W_{xo} * x_t + W_{ho} * H_{t-1} + W_{co} \circ C_t + b_o) \\ H_t = o_t \circ \tanh(C_t) \end{cases}$$

where i_t , f_t , and o_t are the input gate, forget gate and output gate of the convLSTM at time t, respectively. They are three most important parts in the convLSTM because they are designed to overcome gradient exploding and vanishing problems existing in conventional RNN. W and b are the model hyperparameters (weights and biases) that need to be trained for corresponding gates. x_t , C_t and H_t are the input, cell output and hidden state at time t, respectively. Symbols "*" and " \circ " denote the convolution operator and Hadamard product, respectively. σ and \tanh are two different activation functions.

In Figure S2, the cell state C_t can store information over long time periods, making the module good at remembering long-term patterns in spatial-temporal sequences. The forget gate f_t controls the flow of information from previous cell states C_{t-1} and determine when to remember or forget information. The input gate i_t controls the flow of information from the cell activation. The hidden state H_t is obtained from the output gate o_t and current cell state C_t .

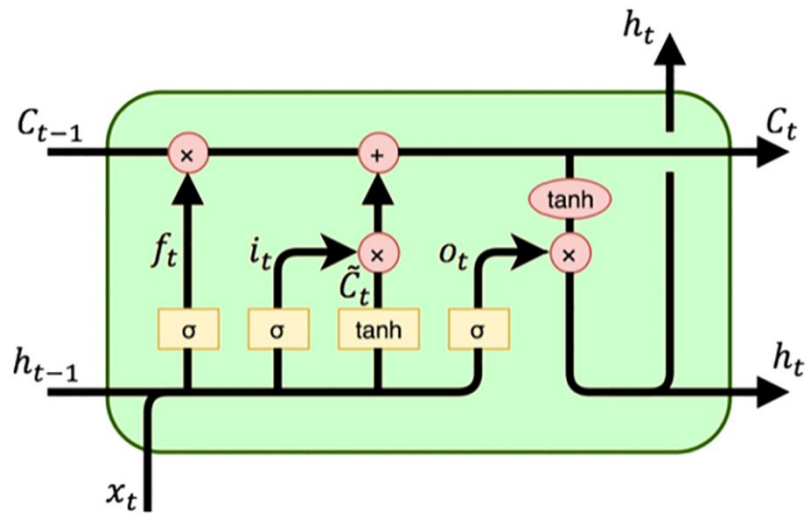


Figure S1. The architecture of convLSTM module (<https://colah.github.io/posts/2015-08-Understanding-LSTMs/>).

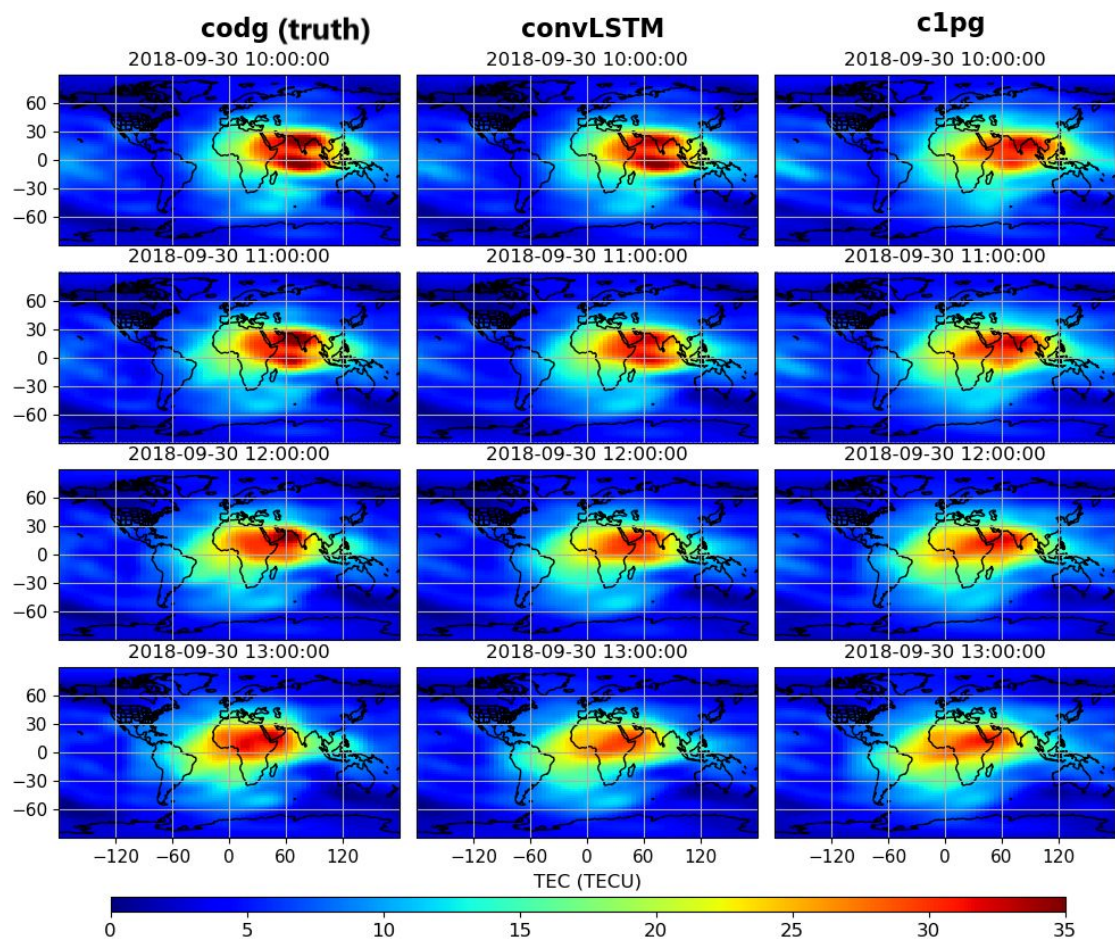


Figure S2. Same as Figure 4 but for the quiet time (10:00-13:00 UT, September 30, 2018), where the KP varies from 1 to 0.7, and F10.7 is 68.5.